

SCIENTIFIC REPORTS



OPEN

Facile control of nanoporosity in Cellulose Acetate using Nickel(II) nitrate additive and water pressure treatment for highly efficient battery gel separators

Woong Gi Lee¹, Do Hyeong Kim², Woo Cheol Jeon², Sang Kyu Kwak^{1,2}, Seok Ju Kang^{1,2} & Sang Wook Kang¹

We succeed in fabricating nearly straight nanopores in cellulose acetate (CA) polymers for use as battery gel separators by utilizing an inorganic hexahydrate ($\text{Ni}(\text{NO}_3)_2 \cdot 6\text{H}_2\text{O}$) complex and isostatic water pressure treatment. The continuous nanopores are generated when the polymer film is exposed to isostatic water pressure after complexing the nickel(II) nitrate hexahydrate ($\text{Ni}(\text{NO}_3)_2 \cdot 6\text{H}_2\text{O}$) with the CA. These results can be attributed to the manner in which the polymer chains are weakened because of the plasticization effect of the $\text{Ni}(\text{NO}_3)_2 \cdot 6\text{H}_2\text{O}$ that is incorporated into the CA. Furthermore, we performed extensive molecular dynamics simulation for confirming the interaction between electrolyte and CA separator. The well controlled CA membrane after water pressure treatment enables fabrication of highly reliable cell by utilizing 2032-type coin cell structure. The resulting cell performance exhibits not only the effect of the physical morphology of CA separator, but also the chemical interaction of electrolyte with CA polymer which facilitates the Li-ion in the cell.

Porous materials – and in particular nanoporous membranes – have been widely used in various nano- and bio-technology applications such as gas storage, filters, battery separators, polymer electrolyte membranes, polymer support, and water treatment or purification^{1–8}. Specifically for battery separators, porous organic materials have become promising candidates for highly efficient lithium (Li)-ion or lithium-metal battery applications because of the fact that their morphologies can be easily tuned by using smart functional materials and chemistry^{9–12}. Thus, it has been intensively studied to further improve battery performance with advanced anode and cathodes materials^{13–15}. For example, previous work by T. C. Mike Chung research group suggested a new class of polyethylene-based anion exchange membrane (PE-AEMs) as separator of lithium ion battery. The PE-AEMs has contained flexible ammonium chloride ($-\text{NR}_3^+\text{Cl}^-$) and a cross-linking PE network structure. The properties of this membrane show high thermal stability, including adequate water swelling, and exceptionally high ionic-conductivity of 119.6 mS/cm in 2N HCl solution and 78.8 mS/cm in 2N HCl-0.2N CuCl solution¹⁶. Also, Zhuyi Wang research group suggested an organic-inorganic hybrid multilayer battery separator using by layer-by-layer (LbL) self-assembly process. The formation of functional ultrathin multilayer on PE separator exhibited high performance battery properties^{17,18}. In addition, the porous separators of battery have been fabricated through a variety of methods, such as thermally induced phase separation, phase inversion, and track-etching, anodization and blade casting process^{19–29}. However, certain vexing problems accompany these methods, which include complicated procedures and high-cost processes for mass production; such obstacles are not desirable in battery separator applications.

¹Department of Chemistry, Sangmyung University, Seoul, 110-743, Republic of Korea. ²School of Energy and Chemical Engineering, Ulsan National Institute of Science and Technology (UNIST), Ulsan, 689-798, Republic of Korea. Woong Gi Lee and Do Hyeong Kim contributed equally to this work. Correspondence and requests for materials should be addressed to S.K.K. (email: skkwak@unist.ac.kr) or S.J.K. (email: sjkang@unist.ac.kr) or S.W.K. (email: swkang@smu.ac.kr)

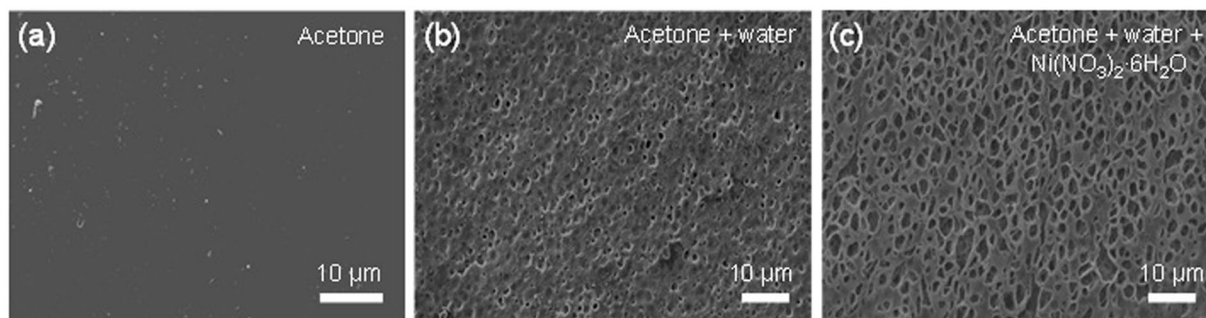


Figure 1. Scanning electron microscopy (SEM) images. (a) Pores observed in a neat cellulose acetate (CA) polymer matrix in acetone. (b) Neat CA polymer matrix in acetone/water (w/w 8:2). (c) 1:0.23 CA/ $\text{Ni}(\text{NO}_3)_2 \cdot 6\text{H}_2\text{O}$ polymer matrix in acetone/water (w/w 8:2).

In order to remedy these issues, simple, low-cost, energy-efficient, and environmentally friendly methods for generating nanopores are needed to generate the polymer separators. Recently, cellulose and its derivative polymer matrix have been studied on account of their various advantages such as high strength, durability, high thermal stability, good biocompatibility, relatively low cost, low density, and good mechanical stability³⁰. However, although such nanopores possess these significant intrinsic advantages, it is still difficult to utilize the nanopores and to obtain a large fabrication area.

In this study, we develop a simple, low-cost, energy-efficient, and environmentally friendly method for fabricating nearly straight nanopores in a thermally stable cellulose acetate (CA) polymer matrix by combining an inorganic complex with isostatic water pressure treatment. The straight-type CA separator and gelation phenomena allow us to achieve stable Li-ion transport. The molecular dynamic (MD) simulation also reveals that electrolytes can easily diffuse uptake into the CA separator, resulting in decrease of the resistance in the battery cell. Furthermore, we demonstrate a Li-ion half-cell battery with a LTO electrode. The half cell with a well-controlled CA separator exhibits stable electrochemistry without any serious degradation in battery performance.

Results and Discussion

Surface morphology. Scanning electron microscopy (SEM) was used to investigate the pores generated in the CA polymer matrix using pure acetone, acetone/water (w/w 8:2), and acetone/water (w/w 8:2) with a $\text{Ni}(\text{NO}_3)_2 \cdot 6\text{H}_2\text{O}$ additive. Figure 1(a) shows the surface morphology of neat CA, which was dissolved in pure acetone. The SEM image clearly demonstrates that there are no pores on the surface of the CA polymer dissolved in pure acetone. By way of contrast, for the CA polymer matrix dissolved in the acetone/water co-solvent, pores were generated on the surface, as shown in Fig. 1(b). The pores had a radius of approximately $1\ \mu\text{m}$ and were homogeneously distributed on the surface mainly owing to the presence of the high boiling point of water molecules in the solution during the film formation.

Although the acetone/water co-solvent generates pores on the CA polymer matrix, it is still difficult to control the size and porosity of the pores during membrane formation. Therefore, in order to control the pore size of the CA membrane, we introduced a new approach that incorporates $\text{Ni}(\text{NO}_3)_2 \cdot 6\text{H}_2\text{O}$ into the acetone/water blend solvent. The resulting SEM image shows that the pore size and porosity of the polymer matrix dramatically increased on the CA polymer surface. It should be noted that there are two major plausible explanations for why the larger pores were formed in the CA membrane. i) The solvated $\text{Ni}(\text{NO}_3)_2 \cdot 6\text{H}_2\text{O}$ aggregates in the polymer matrix during solidification, while the volatile acetone rapidly evaporates; this results in the remaining $\text{Ni}(\text{NO}_3)_2 \cdot 6\text{H}_2\text{O}$ aggregates forming well-defined pores in the CA polymer matrix. ii) There is strong molecular-level ionic association between Ni, nitrate, and water molecules. This strong interaction retards the evaporation of water molecules in the CA polymer matrix, which results in the formation of pores on the surface.

Pressure effect on polymer matrix. To further increase the pore size, 1:0.23 CA/ $\text{Ni}(\text{NO}_3)_2 \cdot 6\text{H}_2\text{O}$ polymer matrix films were examined as a function of isostatic water pressure, which ranged from 2 to 8 bar. The dried polymer matrix containing $\text{Ni}(\text{NO}_3)_2 \cdot 6\text{H}_2\text{O}$ was placed in water-treatment equipment and then subjected to water pressures ranging from 2 to 8 bar. Figure 2 shows a graph of the flux as a function of water pressure after the water pressure treatment. The graph illustrates that there is no significant water flux until the water pressure reaches 2 bar. From this point, for water pressures beyond 3 bar, the flux monotonically increases as a function of water pressure. The primary explanation for the increased pore size as a function of water pressure is that the CA chains, which were weakened by the $\text{Ni}(\text{NO}_3)_2 \cdot 6\text{H}_2\text{O}$ solvate, were torn by the high pressure. This results in a well-defined channel, as shown in Fig. 3(a). It was thought that the mobility of $\text{Ni}(\text{NO}_3)_2 \cdot 6\text{H}_2\text{O}$ in CA polymer could provide the space to be freely moved for polymer chains, resulting in the plasticization effect to increase the free volume. Thus, this plasticization effect plays a critical role in generating interconnected pores. Figure 3(b–d) shows SEM images of the pores generated in 1:0.23 CA/ $\text{Ni}(\text{NO}_3)_2 \cdot 6\text{H}_2\text{O}$ matrices at water pressures of 5 bar and 8 bar (Supplementary Fig. S1), respectively.

Plasticization effect. In order to further understand the plasticization effect of $\text{Ni}(\text{NO}_3)_2 \cdot 6\text{H}_2\text{O}$ solvates with CA chains during the water treatment process, we obtained FT-IR spectra by using a VERTEX 70

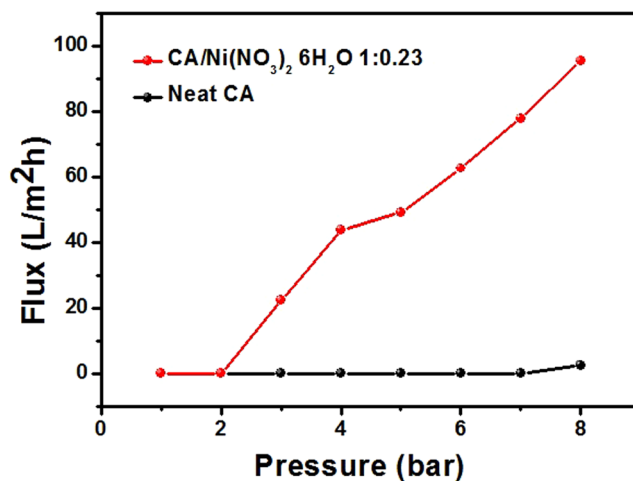


Figure 2. Flux measured through neat cellulose acetate (CA) and CA with $\text{Ni}(\text{NO}_3)_2 \cdot 6\text{H}_2\text{O}$ at various water pressures.

FT-IR spectrometer (Bruker Optics Inc.). Figure 4 shows the FT-IR spectra of neat CA as well as 1:0.23 CA/ $\text{Ni}(\text{NO}_3)_2 \cdot 6\text{H}_2\text{O}$ at water pressures of 0 bar and 8 bar. The neat CA polymer matrix sample exhibits the characteristic IR peak at 3478 cm^{-1} , which corresponds to the hydroxyl group of the CA polymer. By way of contrast, the sample with $\text{Ni}(\text{NO}_3)_2 \cdot 6\text{H}_2\text{O}$ solvates shows representative absorption bands for CA/ $\text{Ni}(\text{NO}_3)_2 \cdot 6\text{H}_2\text{O}$ at 3422 cm^{-1} because of the abundance of H_2O molecules in $\text{Ni}(\text{NO}_3)_2 \cdot 6\text{H}_2\text{O}$, which cause the intensity of the OH adsorption peak to increase. The subsequent water pressure to the CA polymer sample at 8 bar. The peak observed at the 3422 cm^{-1} for CA/ $\text{Ni}(\text{NO}_3)_2 \cdot 6\text{H}_2\text{O}$ shifted to 3478 cm^{-1} , indicating that a considerable amount of $\text{Ni}(\text{NO}_3)_2 \cdot 6\text{H}_2\text{O}$ was removed by the high-water-pressure treatment.

Porosity of the CA polymer. In order to quantitatively measure the increased pore size and porosity of the CA polymer matrix, we utilized a mercury porosimeter (Autopore IV9500 model, Micromeritics Inc.). Figure 5(a) and (b) show the pore size of the CA polymer matrix without $\text{Ni}(\text{NO}_3)_2$ and with the $\text{Ni}(\text{NO}_3)_2$ additive. The dominant pore size of the CA polymer without $\text{Ni}(\text{NO}_3)_2$ shows a sharp peak at 120 nm; However, the sample with the $\text{Ni}(\text{NO}_3)_2$ additive exhibits a broad band around a few hundred nanometers, implying that the $\text{Ni}(\text{NO}_3)_2$ additive broadens the pore size in the CA polymer matrix. We observed larger pore sizes and volumes from water pressure samples with the $\text{Ni}(\text{NO}_3)_2$ additive, as shown in Fig. 5(c–e). We can conclude from these data that the pore size and volume increased considerably from the water pressure treatment for the polymer matrix that contained the $\text{Ni}(\text{NO}_3)_2$ additive.

Interaction between CA polymer and electrolyte. To apply the CA polymer matrix in battery separator, the interacting preference between CA and electrolytes (ethylene carbonate (EC), and diethyl carbonate (DEC)) were further investigated by Flory-Huggins (FH) interaction parameter^{31,32} (χ) calculated by using Hildebrand solubility parameter³³ (δ) (Supplementary Note 1 in Supplementary information). Three different temperatures of 298 K, 323 K and 363 K were considered representing room temperature, battery heating temperature³⁴, and simulation temperature. According to Flory-Huggins theory^{31,32}, when χ value goes to zero, the constituent materials have better compatibility and higher affinity. In other words, smaller χ value indicates that two constituent materials are thermodynamically more miscible and this phenomenon is decisively referred by similar δ values of the materials. Note that the last temperature was set to expedite molecular dynamics (MD) for a rapid observation of the time-dependent phase of the system. Table 1 shows calculated Hildebrand solubility parameters and FH parameters among CA, EC and DEC. $\chi_{\text{CA-EC}}$ was decreased as temperature was increased. It indicates that CA and EC are more miscible at high temperature. On the other hand, $\chi_{\text{CA-DEC}}$ followed an opposite behavior, where CA and DEC are more immiscible at elevated temperature. Finally, $\chi_{\text{EC-DEC}}$ showed the same behavior as $\chi_{\text{CA-EC}}$ yet the larger values compared to $\chi_{\text{CA-EC}}$ and $\chi_{\text{CA-DEC}}$ were indicative of partial unmixing.

Based on the miscibility predicted by the FH parameters, the layered model system of CA and EC/DEC was constructed to investigate the intermixing dynamics of the components. Figure 6 shows the model system and the results of MD simulation at 363 K and 1 atm (see MD simulation in Methods). At early stage, both EC and DEC started diffusing into CA together. As time passed, EC diffused into CA while DEC was away from CA as predicted by the characteristic behavior of FH parameters. Note that the same phenomenon was observed with 30mer CA (Fig. 7). More notably, the diffusivity of CA, which was obtained from additional MD simulation (Supplementary Note 2 in Supplementary information), revealed that the diffusivity in the layered system ($\sim 1.21 \times 10^{-14}\text{ cm}^2/\text{s}$) was two orders of magnitude greater than that in the bulk phase ($\sim 1.54 \times 10^{-16}\text{ cm}^2/\text{s}$). The result indicated that the presence of EC/DEC induced the free movement of CA. Thus, we conjecture that the gel-like phase of CA might appear due to the active inter-diffusion of EC/DEC during the battery operation.

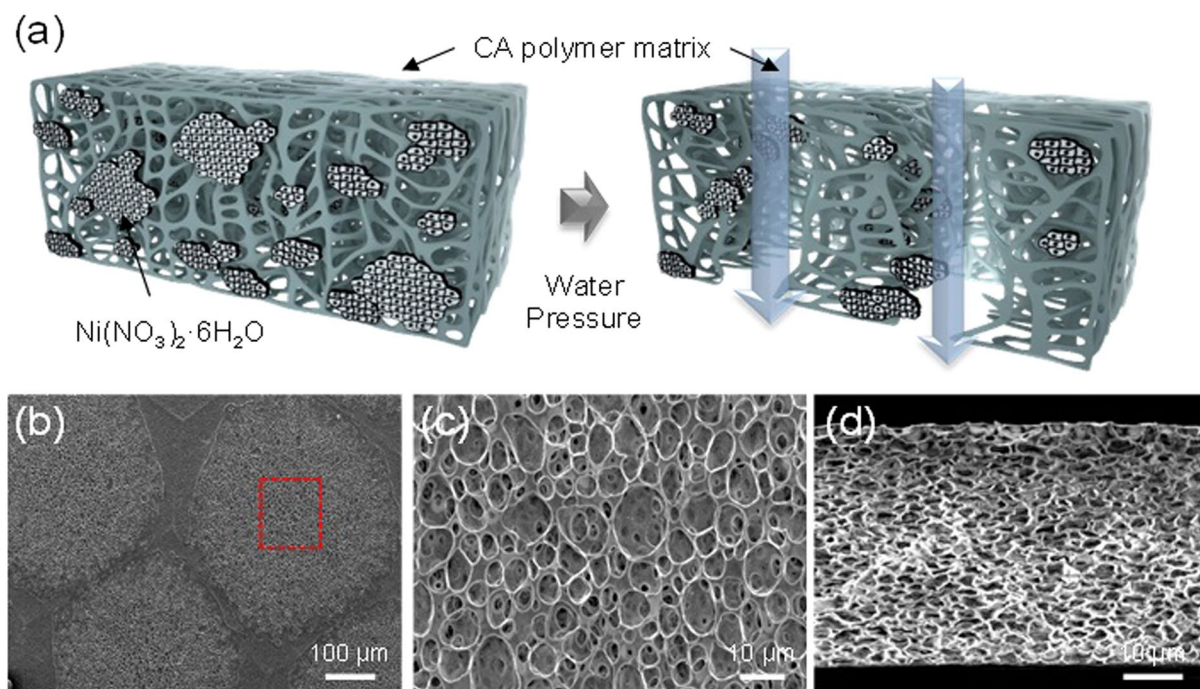


Figure 3. (a) Schematic diagram of the proposed nanoporous (CA) polymer. Top view (SEM) images of CA surface morphology observed in 1:0.23 CA/ $\text{Ni}(\text{NO}_3)_2 \cdot 6\text{H}_2\text{O}$ in acetone/water (w/w 8:2) at water pressures of 5 bar (b). The red dashed squares in (b) indicate the magnified areas shown in panes, respectively (c). Cross-sectional views of the samples subjected to water pressures of 5 bar (d).

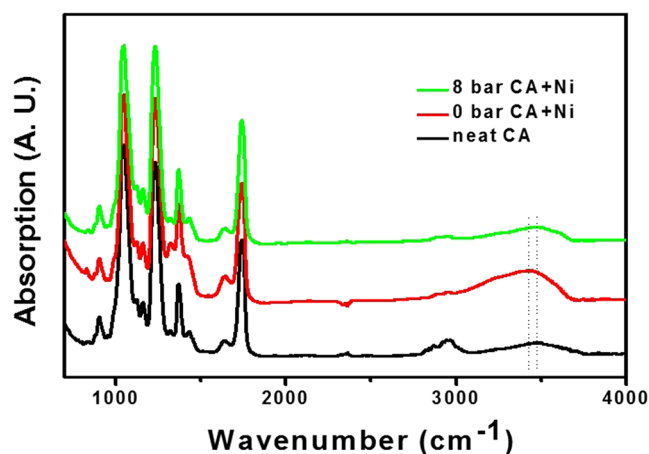


Figure 4. Fourier transform infrared (FT-IR) spectra of neat cellulose acetate (CA) and the 1:0.23 CA/ $\text{Ni}(\text{NO}_3)_2 \cdot 6\text{H}_2\text{O}$ polymer matrix at water pressures of 0 bar and 8 bar.

Thermal stability of CA polymer. TGA was carried out to confirm the thermal stability of the porous polymer matrix using a Universal V4.5 A (TA Instruments). Figure 8 shows that about 90 wt% of neat CA and CA incorporated with $\text{Ni}(\text{NO}_3)_2 \cdot 6\text{H}_2\text{O}$ at 8 bar were decomposed at around 300 °C. On the other hand, about 80 wt% of CA with $\text{Ni}(\text{NO}_3)_2 \cdot 6\text{H}_2\text{O}$ at 0 bar was decomposed between 200 and 350 °C, and 2 wt% was decomposed between 350 and 550 °C. The boiling point of $\text{Ni}(\text{NO}_3)_2 \cdot 6\text{H}_2\text{O}$ is 136.7 °C. It was estimated that polymer chains were loosened by the solvated $\text{Ni}(\text{NO}_3)_2 \cdot 6\text{H}_2\text{O}$ in the polymer chains. Thus, the loss of about 80 wt% CA with $\text{Ni}(\text{NO}_3)_2 \cdot 6\text{H}_2\text{O}$ can be attributed to the degradation of solvated $\text{Ni}(\text{NO}_3)_2 \cdot 6\text{H}_2\text{O}$ and the loosened polymer chain. However, the thermal stability of the polymer matrix increased as a result of the water treatment. This increase in thermal stability can be explained by the fact that most $\text{Ni}(\text{NO}_3)_2 \cdot 6\text{H}_2\text{O}$ was removed from the CA polymer. Furthermore, it was confirmed that the little remaining $\text{Ni}(\text{NO}_3)_2 \cdot 6\text{H}_2\text{O}$ was decomposed above 400 °C.

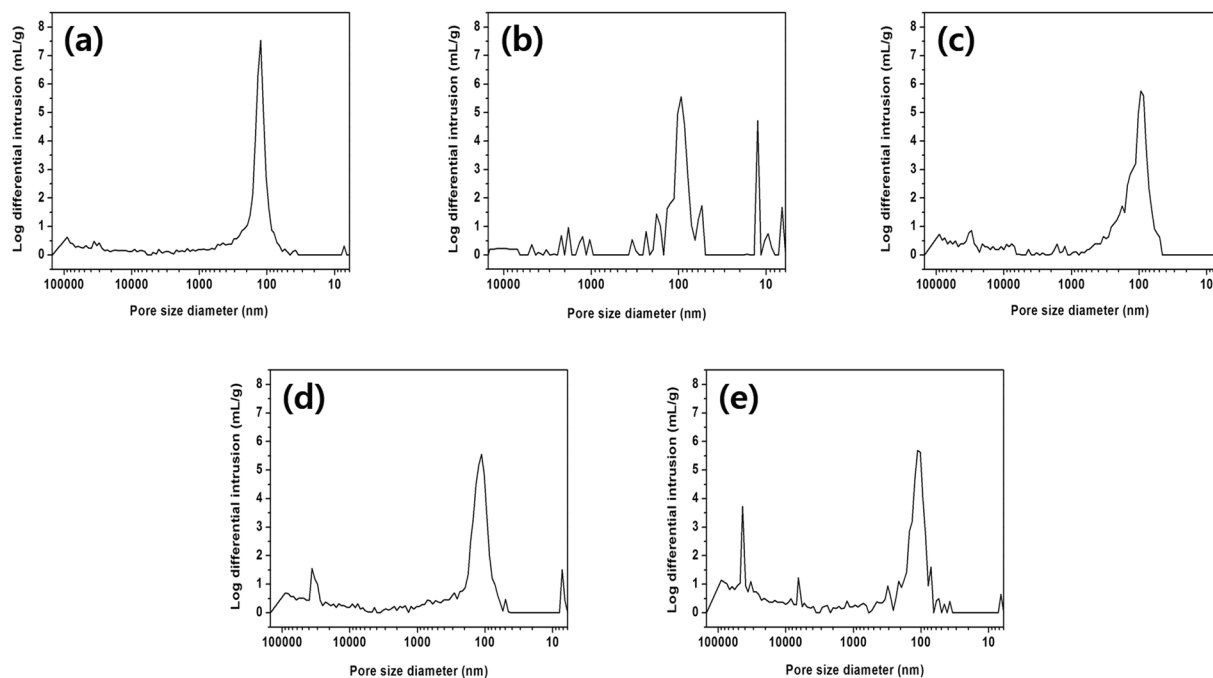


Figure 5. Porosimeter data. (a) Porosity in a neat cellulose acetate (CA) polymer matrix at a water pressure of 0 bar. Porosity in a 1:0.23 CA/Ni(NO₃)₂ polymer matrix at water pressures of (b) 0 bar, (c) 2 bar, (d) 5 bar, and (e) 8 bar.

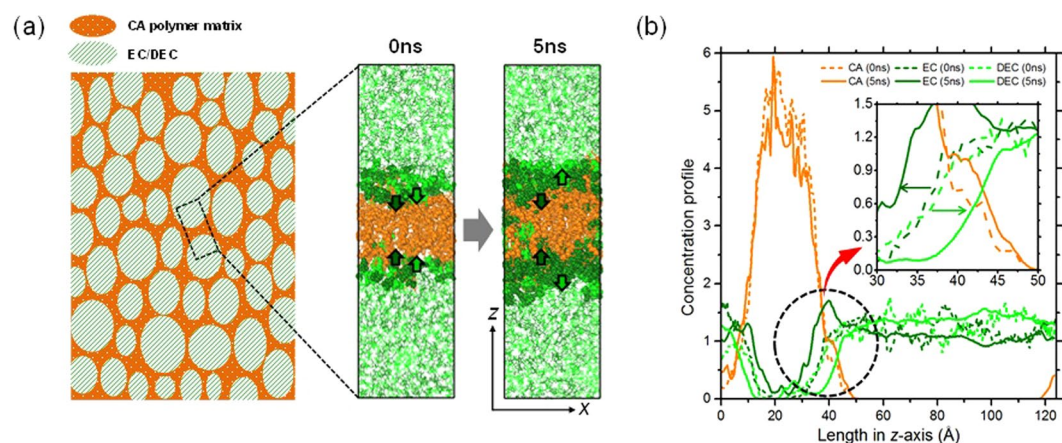


Figure 6. (a) Schematic diagrams of cross-section of CA polymer matrix with EC/DEC liquid mixture. The vol% ratio of CA to EC/DEC is 20:80, where that of EC to DEC is 50:50. Snapshots of MD simulations, which are presented on the left, show the initial (0 ns) and final (5 ns) states of the system. Dark green and light green arrows indicate the diffusion of EC and DEC molecules, respectively. (b) Concentration profiles of CA, EC, and DEC of the initial (0 ns) and final (5 ns) states of the layered system. Orange, dark green and light green colors represent CA, EC, and DEC molecules, respectively.

Temperature (K)	δ_{CA} (J/cm ³) ^{0.5}	δ_{EC} (J/cm ³) ^{0.5}	δ_{DEC} (J/cm ³) ^{0.5}	χ_{CA-EC}	χ_{CA-DEC}	χ_{EC-DEC}
298	26.2(24.5)	30.0(29.6)	18.7(18.0)	0.37	2.81	6.30
323	25.9	29.3	18.1	0.27	2.91	5.92
363	25.6	28.2	17.1	0.16	3.14	5.41

Table 1. Hildebrand solubility parameters (δ) and Flory-Huggins interaction parameters (χ_{ij} 's). The values in parentheses are from Hansen³⁷ and the average error percent is about ~4.2%.

Electrochemical characteristic. The precisely controlled pore size of our CA polymer separators was characterized by the galvanostatic plating/stripping method from stacked Li metal/CA separator (after water pressure

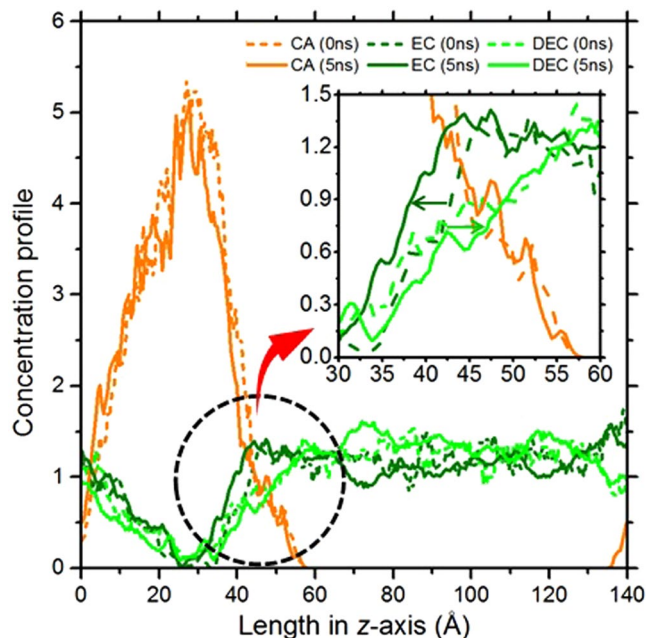


Figure 7. Concentration profiles of CA, EC, and DEC of the initial (0 ns) and final (5 ns) states of the layered system.

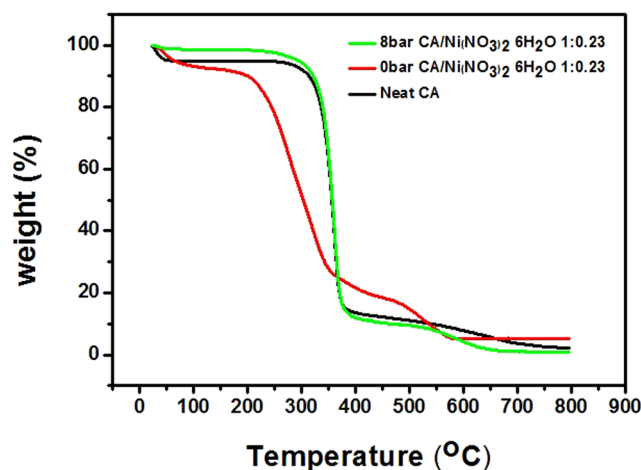


Figure 8. Thermogravimetric analysis (TGA) of neat cellulose acetate (CA) and CA/ Ni(NO₃)₂·6H₂O polymer matrix at water pressures of 0 bar and 8 bar.

treatment)/Li Metal architecture, as shown in Fig. 9(a). For electrochemical measurements, a relatively low pressurized CA separator was applied because a high water pressure sample (ie 8 bar) often foamed unexpected large pores during the process. 1.3 M lithium hexafluorophosphate (LiPF₆) in EC/DEC (50 v/50 v) with 10% FEC additive was used as an electrolyte for the cell test. In order to measure the electrochemical characteristics in the symmetry cells, we initially plated 0.5 C Li metal on the working electrode and stripped the same amount with a galvanostatic current of ± 0.5 mA (Fig. 9(a)). Figure 9(b) shows the plating/stripping cycle potential profiles containing polymeric and CA separator after water pressure treatment at 2 bar. The polymeric Celgard separator shows a higher plating/stripping potential than the symmetry cell with the CA separator after water pressure treatment at 2 bar. In addition, the electrochemical impedance measurements of CA separator in Fig. 9(c) exhibit smaller passivation and charge transfer resistance than that of polymeric separator, indicating that the CA separator can effectively lower the resistance in the Li/Li symmetry cell system.

To extend our new CA separator for more realistic battery applications, we constructed a LTO/ CA separator (after water pressure treatment) /Li metal configuration battery with 1.3 M LiPF₆ in EC/DEC (50 v/50 v) with a 10% FEC additive electrolyte, as shown in Fig. 9(d). The galvanostatic discharge/charge profile clearly exhibits stable discharging/charging plateaus at 1.54 V and 1.58 V, respectively (Fig. 9(e)). Using this half-cell configuration, we were also able to measure the various current rates from 1 C to 15 C, as shown in Fig. 9(f). Upon increasing

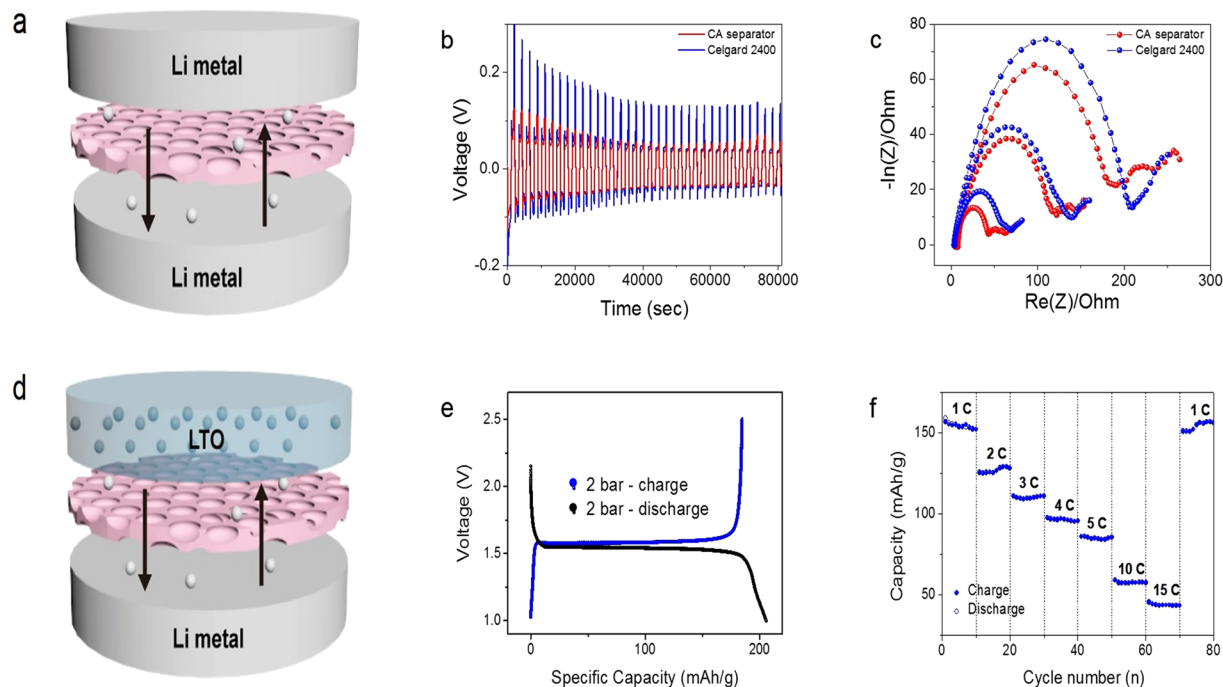


Figure 9. (a) Schematic representation of the Li metal/cellulose acetate (CA) separator/ Li metal symmetry cell architecture. (b) chronopotentiometry results of symmetry cell with the polymeric Celgard separator (blue line) and the 1:0.23 CA/Ni(NO₃)₂ polymer separator at a water pressure of 2 bar (red line). (c) The Nyquist plots of symmetry cells with Celgard (blue dots) and CA (red dots) separators as a function of cycle number (d) Schematic representation of the Li metal/CA separator/LTO half-cell architecture. (e) Galvanostatic discharge-charge profiles of half-cell with the 1:0.23 CA/Ni(NO₃)₂ polymer separator at a water pressure of 2 bar. (f) Rate performance of Li metal/CA separator/LTO half-cell.

the current rate of the cell, the average capacity monotonically decreased from 160 mAh/g to 50 mAh/g and completely recovered the average capacity at a 1 C rate. This stable battery operation suggests that the CA separator after water pressure treatment of 2 bar can sustain Li-ion exchange in the cell even at high current densities.

In conclusion, we utilized an inorganic complex in concert with isostatic water pressure treatment for a CA polymer. We found that when the CA/Ni(NO₃)₂·6H₂O complex film was exposed to isostatic water pressure, continuous nanopores were generated in the polymer. The generated nanopores could be explained by the weakened polymer chains, which resulted from the plasticization effect of the incorporated Ni(NO₃)₂·6H₂O into CA, resulting in the interconnected pores when water pressure was applied. The high electrolyte uptake ability of nanoporous CA polymer is carefully confirmed by experimental and MD simulation. Such a high Li affinity in CA separator allows stable Li-ion transfer in the half cell structure.

Methods

Separator fabrication. A 10% (w/w) solution of CA was obtained by dissolving CA in acetone/water (w/w 8:2). To prepare the polymer matrix, the amount of nickel(II) nitrate hexahydrate (Ni(NO₃)₂·6H₂O) added to the polymer matrix was determined according to the mole ratio of the Ni ion to the monomeric unit of CA. At this stage, the final mixture was stirred for 2 h at room temperature. Subsequently, the solutions were cast about 200 μm thickness by using doctor blade to form a freestanding film on a glass plate and dried under atmospheric pressure for 12 h. The dried polymer matrix containing Ni(NO₃)₂·6H₂O was then subjected to water pressures ranging from 2 to 8 bar. The water flux of the films with varying porosities was measured and expressed in units of L/m²h.

Symmetry and half cell fabrication. The battery-grade 1.3 M LiPF₆-EC/DEC (ethylene carbonate/diethyl carbonate) with a 10 wt% fluoroethylene carbonate (FEC) electrolyte was used for both the symmetry and half cell. The 300 μm thick pure Li metal and 5 μm thick Li metal on Cu foil were purchased from Wellcos Co. and Sidrabe Co., respectively. The active electrodes consisted of LTO, PVDF, and Super P (8:1:1) and were dissolved in NMP and subsequently coated on a Cu foil. The active electrodes were dried in a vacuum oven at 80 °C for 12 h. The PS (Celgard® 2400) separator was used as a reference separator. The 2032-type coin cells were used for symmetry and half-cell measurements. The coin cells were pressurized by using a crimping machine (Hohsen Corp). The battery cells were prepared in an Ar-filled glove box (<0.1 ppm O₂ and H₂O).

MD simulation. For the molecular dynamics (MD) study, CA, EC and DEC were modeled (Figure S2 and Table S1) and two individual system of CA and a mixture of EC/DEC were separately constructed with 5 of 20

mer CA polymer and with 564 of EC and 310 of DEC molecules, respectively. Each system was relaxed with NPT (i.e. isothermal-isobaric ensemble) MD for 500 ps with the time step of 0.5 fs. Note that temperatures were set to be 500 K for annealing CA and 363 K for relaxing the EC/DEC mixture. Then, the two systems were systematically put together into the periodic box with the size of $40.6 \times 40.6 \times 137.1 \text{ \AA}^3$, which was subsequently relaxed by NPT MD for another 500 ps at 500 K and 1 atm. Finally, the layered system (Figs 6 and 7) was performed with NPT MD for 5 ns with the time step of 1 fs at 363 K and 1 atm. For the MD simulations, COMPASS II forcefield was used^{35,36}.

Characterization. Fourier transform infrared (FT-IR) measurements were performed on a Varian FTS3100 spectrometer; 64–200 scans were averaged at a resolution of 4 cm^{-1} . Thermogravimetric analysis (TGA) was performed with Mettler Toledo TGA devices at a heating rate of $10^\circ\text{C}/\text{min}$. Scanning electron microscopy (SEM, JSM-5600LV, JEOL) was used to investigate the pores generated in the polymer. Additionally, a mercury porosimeter (Autopore IV9500 model, Micromeritics Inc.) was used to analyze the pore size and porosity generated in the polymer matrix. Electrochemical experiments were performed using a BioLogic VMP3 or a WonATech battery tester (WBCS3000L).

References

- Sunho, C. *et al.* Modification of the Mg/DOBDC MOF with Amines to Enhance CO_2 Adsorption from Ultradilute Gases. *J. Phys. Chem. Lett.* **3**(9), 1136–1141, doi:10.1021/jz300328j (2012).
- Dalal, A. *et al.* MOF Crystal Chemistry Paving the Way to Gas Storage Needs: Aluminum-Based MOF for CH_4 , O_2 , and CO_2 Storage. *J. Am. Chem. Soc.* **137**(41), 13308–13318, doi:10.1021/jacs.5b07053 (2015).
- Zhenxia, Z. *et al.* Gas Separation Properties of Metal Organic Framework(MOF-5) Membranes. *Ind. Eng. Chem. Res.* **52**(3), 1102–1108, doi:10.1021/ie202777q (2013).
- Bo, L., Hiroshi, S., Tomoki, A. & Qiang, X. Metal-Organic Framework as a Template for Porous Carbon Synthesis. *J. Am. Chem. Soc.* **130**(16), 5390–5391, doi:10.1021/ja7106146 (2008).
- Serena, M. *et al.* Hydrophilic porous asymmetric ultrafiltration membranes of aramid-g-PEO copolymer. *J. Membr. Sci.* **454**, 233–242 (2001).
- Mark, A. S. *et al.* Science and technology for water purification in the coming decades. *Nature* **452**, 301–310, doi:10.1038/nature06599 (2008).
- Yusong, Z. *et al.* Trilayer poly(vinylidene fluoride)/polyborate/poly(vinylidene fluoride) gel polymer electrolyte with good performance for lithium ion batteries. *J. Mater. Chem.* **1**, 7790–7797, doi:10.1039/c3ta00167a (2013).
- Vela, M. C. V., Silvia, A. B., Jami, L. G. & Enrique, B. R. Analysis of membrane pore blocking models adapted to cross flow ultrafiltration in the ultrafiltration of PEG. *J. Chem. Eng.* **149**, 232–241, doi:10.1016/j.ccej.2008.10.027 (2009).
- Je Hyoun, O., Young Soo, K. & Sang Wook, K. Poly(vinylpyrrolidone)/KF electrolyte membrane for facilitated CO_2 transport. *J. Chem. Commun.* **49**(86), 10181–10183, doi:10.1039/c3cc46253f (2013).
- Da Eun, S., Young Soo, K. & Sang Wook, K. Highly permeable and stabilized olefin transport membranes based on a poly(ethylene oxide) matrix and $\text{Al}(\text{NO}_3)_3$. *J. Membr. Sci.* **474**, 273–276, doi:10.1016/j.memsci.2014.09.050 (2015).
- Yun, L. *et al.* Composite porous membranes with an ultrathin selective layer for vanadium flow batteries. *J. Chem. Commun.* **50**, 4596–4599, doi:10.1039/c3cc49729a (2014).
- Carlos, M. C., Maria, M. S. & Lanceros-Mendez, S. Battery separators based on vinylidene fluoride (VDF) polymer and copolymers for lithium ion battery applications. *J. RSC. Adv.* **3**, 11404–11417, doi:10.1039/c3ra40732b (2013).
- Lishuang, F. *et al.* Graphene Aerogels with Anchored Sub-Micrometer Mulberry-Like ZnO Particles for High-Rate and Long-Cycle Anode Materials in Lithium Ion Batteries. *Small* **12**, 5208–5216, doi:10.1002/sml.v12.37 (2016).
- Lishuang, F., Bingjiang, L., David, W. R., Naiqing, Z. & Kening, S. *In situ* Preparation of 3D Graphene Aerogels@Hierarchical Fe_3O_4 Nanoclusters as High Rate and Long Cycle anode Materials for Lithium Ion Batteries. *Chem. Commun.* **51**, 1597–1660, doi:10.1039/C4CC08949A (2015).
- Vinodkumar, E. *et al.* Challenges in the Development of Advanced Li-ion Batteries: a Review. *Energy Environ. Sci.* **4**, 3243–3262, doi:10.1039/c1ee01598b (2011).
- Min, Z. *et al.* New polyethylene based anion exchange membranes (PE-AEMs) with high ionic conductivity. *Macromolecules* **44**(15), 5937–5946, doi:10.1021/ma200836d (2011).
- Wuxia, X. *et al.* Layer-by-layer deposition of organic-inorganic hybrid multilayer on microporous polyethylene separator to enhance the electrochemical performance of lithium-ion battery. *ACS Appl. Mater. Interfaces* **7**, 20678–20686, doi:10.1021/acsami.5b05457 (2015).
- Sheng-Heng, C. & Arumugam, M. High-permeance Li-S batteries with an ultra-lightweight MWCNT-coated separator. *J. Phys. Chem. Lett.* **5**, 1978–1983, doi:10.1021/jz5006913 (2014).
- Xiaoming, H. *et al.* Ultrastrong Polyoxazole Nanofiber Membranes for Dendrite-Proof and Heat-Resistant Battery Separators. *Nano Lett.* **16**, 2981–2987, doi:10.1021/acs.nanolett.5b05133 (2016).
- Douglas, R. L., Kim, S. S. & Kevin, E. K. Microporous membrane formation via thermally induced phase separation. II. *Liquid-liquid phase separation*, *J. Membr. Sci.* **64**, 1–11 (1991).
- Kim, S. S. & Douglas, R. L. Microporous membrane formation via thermally-induced phase separation. III. Effect of thermodynamic interactions on the structure of isotactic polypropylene membrane. *J. Membr. Sci.* **64**, 13–29, doi:10.1016/0376-7388(91)80074-G (1991).
- Kim, S. S. *et al.* Microporous membrane formation via thermally-induced phase separation. V. Effect of diluents mobility and crystallization on the structure of isotactic polypropylene membranes. *J. Membr. Sci.* **64**, 41–53, doi:10.1016/0376-7388(91)80076-I (1991).
- Cha, B. J. *et al.* The effects of diluents molecular weight on the structure of thermally-induced phase separation membrane. *J. Membr. Sci.* **108**, 219–229, doi:10.1016/0376-7388 (1995). (95)00171-9.
- Kim, L. U. & Kim, C. K. A Novel method for the pore size control of the battery separator using the phase instability of the ternary mixtures. *J. Membr. Sci. Part B* **44**, 2025–2034, doi:10.1002/(ISSN)1099-0488 (2006).
- Xiaolong, L. & Xianfeng, L. Preparation of polyvinylidene fluoride membrane via a thermally induced phase separation using a mixed diluent. *J. Appl. Polym. Sci.* **114**, 1213–1219, doi:10.1002/app.v114:2 (2009).
- Wentao, Y. *et al.* Study on the control of pore size of membrane using chemical methods part IV. The role of organic acids. *Desalination* **324**, 57–64, doi:10.1016/j.desal.2013.06.002 (2013).
- Reber, N., Kuchel, A., Wolf, A. & Yoshida, M. Transport properties of thermo-responsive ion track membranes. *J. Membr. Sci.* **193**, 49–58, doi:10.1016/S0376-7388(01)00460-4 (2001).
- Husaini, S. N., Zaidi, J. H., Malik, F. & Ariff, M. Application of nuclear track membrane for the reduction of pollutants in the industrial effluent. *Radiat. Meas.* **43**, 607–611, doi:10.1016/j.radmeas.2008.03.070 (2008).

29. Mo, D. *et al.* Fabrication of different pore shapes by multi-step etching technique in ion-irradiated PET membranes. *Nucl. Instrum. Meth. B* **333**, 58–63, doi:10.1016/j.nimb.2014.04.011 (2014).
30. Debashish, R., Mona, S., James, T. G. & Sebastien, P. Cellulose modification by polymer grating: a review. *J. Chem. Soc. Rev.* **7**, 1825–2148 (2009).
31. Flory, P. J. Thermodynamics of High Polymer Solutions. *J. Chem. Phys.* **9**, 660–660, doi:10.1063/1.1750971 (1941).
32. Huggins, M. L. Solutions of Long Chain Compounds. *J. Chem. Phys.* **9**, 440–440, doi:10.1063/1.1750930 (1941).
33. Hildebrand, J. H. & Scott, R. L. The Solubility of Nonelectrolytes, 3rd ed.; Reinhold, New York (1950).
34. Kizilel, R., Sabbah, R., Selman, J. R. & Al-Hallaj, S. An Alternative Cooling System to Enhance the Safety of Li-ion Battery Packs. *J. Power. Sources.* **194**(2), 1105–1112, doi:10.1016/j.jpowsour.2009.06.074 (2009).
35. Jin, S. H., Spenley, N. A., Miller, S. & Todd, S. M. *et al.* COMPASS II: extended coverage for polymer and drug-like molecule databases. *J. Mol. Model.* **22** (2) (2016).
36. Dassault Systemes. Materials Studio 2016; BIOVIA Inc. San Diego, CA, USA (2016).
37. Hansen, C. M. Hansen Solubility Parameters: A User's Handbook, 2nd ed. CRC Press: Boca Raton (2007).

Acknowledgements

This work was supported by an Energy Efficiency & Resources grant from the Korea Institute of Energy Technology Evaluation and Planning (KETEP) (20122010100040), funded by the Ministry of Trade, Industry, and Energy of the Korean Government. This work was also supported by the Basic Science Research Program (2016900369) through the National Research Foundation of Korea (NRF) and funded by the Ministry of Science, ICT, and Future Planning. S.J.K. was supported by the Research Fund of the UNIST in 2016 (1.160102) and Basic Science Research Program through the NRF funded by the Ministry of Education (NRF-2015R1D1A1A02060332). S.K.K. was supported by NRF-2014R1A5A1009799. Computational resources were used from UNIST-HPC, and KISTI-PLSI.

Author Contributions

S.W.K., S.J.K. and S.K.K. led the project, conducted the data analysis and reviewed the manuscript. W.G.L. and D.H.K. performed the experiments, collected the data and wrote the paper. W.C.J. performed the experiments and collected the data.

Additional Information

Supplementary information accompanies this paper at doi:10.1038/s41598-017-01399-8

Competing Interests: The authors declare that they have no competing interests.

Publisher's note: Springer Nature remains neutral with regard to jurisdictional claims in published maps and institutional affiliations.



Open Access This article is licensed under a Creative Commons Attribution 4.0 International License, which permits use, sharing, adaptation, distribution and reproduction in any medium or format, as long as you give appropriate credit to the original author(s) and the source, provide a link to the Creative Commons license, and indicate if changes were made. The images or other third party material in this article are included in the article's Creative Commons license, unless indicated otherwise in a credit line to the material. If material is not included in the article's Creative Commons license and your intended use is not permitted by statutory regulation or exceeds the permitted use, you will need to obtain permission directly from the copyright holder. To view a copy of this license, visit <http://creativecommons.org/licenses/by/4.0/>.

© The Author(s) 2017